Article

Integration of Carbon Dots on Nanoflower Structured ZnCdS as a Cocatalyst for Photocatalytic Degradation

Jie Zhou [1], **Xin Zhao** [1], **Haoming Xu** [1], **Zhichao Wang** [2], **Xiaoyuan Zhang** [1,*] and **Zhiqiang Su** [1,*]

[1] State Key Laboratory of Chemical Resource Engineering, Beijing Key Laboratory of Advanced Functional Polymer Composites, Beijing University of Chemical Technology, Beijing 100029, China
[2] Precision Forestry Key Laboratory of Beijing, Beijing Forestry University, Beijing 100083, China
* Correspondence: 2022500116@buct.edu.cn (X.Z.); suzq@mail.buct.edu.cn (Z.S.)

Abstract: The application of catalysts is one of the most effective methods in the oil refining, chemical, medical, environmental protection, and other industries. In this work, carbon dots (CDs) were selected as an initiator and doped into the main catalyst, $Zn_{0.2}Cd_{0.8}S$, and a novel $Zn_{0.2}Cd_{0.8}S@CD$ composite catalyst with a nanoflower structure was successfully obtained. The synthesized composites ($Zn_{0.2}Cd_{0.8}S@CDs$) were characterized by means of SEM, TEM, XRD, FT-IR, XPS, and UV-Vis DRS. Transient photocurrent response and Nyquist curve analysis further proved that the carrier separation efficiency of the composite catalyst was significantly improved. In addition, the photocatalytic activity of $Zn_{0.2}Cd_{0.8}S@CDs$ for rhodamine B removal from aqueous solution was tested under visible-light irradiation. When the amount of $Zn_{0.2}Cd_{0.8}S@CDs$ composite catalyst reached 50 mg, the degradation rate of rhodamine B was 79.35%. Finally, the photocatalytic degradation mechanism of the $Zn_{0.2}Cd_{0.8}S@CDs$ complex was studied. CD doping enhances the adsorption capacity of $Zn_{0.2}Cd_{0.8}S@CDs$ composite catalysts due to the increase in surface area, effectively inducing charge delocalization and enhancing the photocatalytic capacity. $Zn_{0.2}Cd_{0.8}S@CDs$ composites with low cost and high carrier separation efficiency have broad application prospects in the photocatalytic degradation of dyes.

Keywords: photocatalytic degradation; carbon dots; ZnCdS; nanoflower; rhodamine B

1. Introduction

Rhodamine B (RhB) is a typical cationic organic dye that is mainly used in the fields of printing and dyeing, as well as medicine and steel. When RhB is discharged into water bodies, it turns the color of water purple, making it difficult for sunlight to reach the water, damaging the self-purification ability of the water body, and causing eutrophication [1]. When the human body is exposed to RhB by mistake, it acts on the skin and blood vessels, causing symptoms such as red staining of the skin and internal organs, mild bruising of blood vessels in the brain, fracture of heart muscle fibers, and blurring and disappearance of cross lines [2]. Therefore, it is necessary to treat RhB industrial wastewater before discharge. Methods investigated for the degradation of RhB include chemical oxidation, Fenton reaction, electrochemical oxidation, and photocatalysis. Chemical oxidation [3,4] uses oxidizing agents to oxidize RhB and is prone to secondary contamination; electrochemical oxidation [5,6] is fast and simple but difficult to apply due to high energy and power consumption. Fenton reaction [7–9] and photocatalytic [10–13] methods use generated hydroxyl radicals to oxidize RhB, while photocatalytic method is the most studied of these methods.

$Zn_xCd_{1-x}S$ solid solution is a ternary photocatalyst with a controllable band gap and edge position. It has the advantages of both a narrow band gap of CdS and high stability of ZnS, in addition to good application potential in photocatalysis, especially in hydrogen production. Zeng et al. [14] doped Ag into ZnCdS semiconductor nanocrystals to

improve the optical properties of the composites by mediating the Ag concentration. The addition of Ag precursors affected the relative activity of Zn and Cd precursors. With the increasing band gap of the ZnCdS nanocrystals, the excited Ag Dopant D state shifts to a lower energy level, and the dopant emission also exhibits a blue shift. The photocatalytic properties of single ZnCdS cannot meet the requirements of the present era, so it is urgent to find a composite of ZnCdS and other functional materials to improve the photocatalytic properties [15–17].

Carbon dots (CDs) are nano-sized new materials with excellent optical properties, good water solubility, and low toxicity, that are environmentally friendly, representing a comprehensive source of raw materials that are low-cost, biocompatible, and photoluminescent [18–20]. CDs have excellent electrical conductivity and charge transport ability. CDs can be used as electron donors and electron acceptors, providing a new idea for efficient light energy and catalyst design [21–25]. Their surface can be modified to increase the active sites, benefitting the production of free radicals or proton reduction [15,26–28]. Furthermore, CDs can modulate the band structure of CD-based composites and promote the absorption of light [12,20,21]. Zhu et al. [29] synthesized heteroatom-doped xylose-based carbon (X-CD) and chitosan-based carbon (C-CD) using xylose and chitosan as carbon sources and sulfoxide chloride as a dopant, respectively, to dope S elements. It should be noted that chitosan was used as both a carbon source and an endogenous nitrogen dopant. X-CD doped with only S elements was found to provide more advantages in electron-hole separation because N-related functional groups with strong electron-donating properties weaken the electron capture ability of S-related energy levels.

CDs, serving as an ideal candidate material in the field of energy and the environment, can be used as photocatalysts alone or as auxiliary catalysts for catalytic reactions with a substrate list of semiconductor materials [25,28,30,31] Huang et al. [22] doped CDs in WO_3 nanoplates to construct the interface heterojunction from CDs to WO_3. This electric field drives photoexcited electrons to transmit to CDs, and the remaining photoexcited holes remain on WO_3, thus realizing the space separation of electrons and holes. Teng et al. [32] prepared CDs, MoS_2, and p-C_3N_5 composites with different proportions by hydrothermal and calcination methods. The high charge mobility and high-density hydrogen evolution sites of MoS_2 nanosheets, together with the electronic storage and transfer properties of CDs, can significantly improve the electron transport on the p-C_3N_5 surface and reduce the photogenerated carrier recombination. CDs/MoS_2/p-C_3N_5 composites achieve good photocatalytic performance for hydrogen evolution (H_2) and degradation of methylene blue (MB). Among them, 5% D-MoS_2 (CMSCN5) exhibits the best photocatalytic activity. The hydrogen yield of CMSCN5 is 444 mmol/g·h, which is 1.45 times higher than that of unmodified p-C_3N_5, with an MB removal rate reaching 93.51% within 120 min.

The introduction of N-doped carbon quantum dots (NCQDs) can improve the photocatalytic performance of the catalyst. Xu et al. [33] synthesized NCQDs using g-C_3N_4 as a carbon and nitrogen source. NCQDs with a size of 3.2 nm were prepared by hydrothermal etching and then adsorbed on the surface of CDs with a size of 80 nm to form a strong C-S bond interaction, which induced the surface morphology of CDs to change. NCQDs not only improved the photoabsorption performance of the catalyst but also made the transfer of photogenerated electrons to NCQDs rapid and effective.

In this work, $Zn_{0.2}Cd_{0.8}S$@CD catalysts were prepared by a simple one-pot hydrothermal method. Various characterization methods were applied to study the photocatalytic properties of $Zn_{0.2}Cd_{0.8}S$@CDs and the specific effects of CDs. Some defects of $Zn_{0.2}Cd_{0.8}S$ are remedied by utilizing the relative advantages of CDs, such as unique fluorescence, photoluminescence, conductivity, and charge transfer ability. CDs are small in size, with highly dispersive characteristics, which do not affect the function of photocatalysis but can enhance the properties of $Zn_{0.2}Cd_{0.8}S$ to optimize the photocatalytic performance. In addition, the photocatalytic degradation properties of $Zn_{0.2}Cd_{0.8}S$@CDs were evaluated for rhodamine B (RhB). The results show that the degradation of 10 mg/L RhB solution using a puppy catalyst reached 50.8% within 1 h and 71.36% within 2 h, which superior to

the performance reported in other studies [34–36]. Finally, the photocatalytic degradation mechanism of the $Zn_{0.2}Cd_{0.8}S@CD$ composite photocatalyst was explored.

2. Experiment

2.1. Materials

Citric acid, urea (99.5%), zinc acetate dihydrate (99%), thiourea (99%), sodium sulfate (99%), RhB (96%), potassium bromide (99%), and isopropyl alcohol (99.5%) were purchased from Carbaryl (Shanghai, China). N-dimethylformamide (DMF) (98%), cadmium acetate dihydrate (98%), and Nafion solution were purchased from Tianjin Damao Chemical Plant (Tianjin, China), Thermo Fisher Scientific (Beijing, China) and Tianyu Chemical Technology (Hebei, China), respectively. All of the above reagents were of analytical grade. Deionized water was produced using a Milli-Q system.

2.2. Synthesis of $Zn_{0.2}Cd_{0.8}S$ and $Zn_{0.2}Cd_{0.8}S@CDs$

$Zn_{0.2}Cd_{0.8}S$ was prepared by a facile one-pot hydrothermal method with $Zn(CH_3COO)_2 \cdot 2H_2O$ as a zinc source, $Cd(CH_3COO)_2 \cdot 2H_2O$ as a cadmium source, CH_4N_2S as a sulfur source, and H_2O as a solvent. First, 0.22 g zinc acetate dihydrate, 1.07 g cadmium acetate dihydrate, and 0.38 g thiourea were weighed using an electronic analytical balance and dissolved in 80 mL of ultrapure water. The solution was homogenized by agitation and ultrasound and transferred to the polytetrafluoroethylene (PTFE) lining of a reactor. The reactor was placed in an oven at a temperature of 140 °C for 4 h. After the end of the reaction, the reactor was cooled, and the liquid was removed and centrifuged with a low-speed centrifuge. Then, the resulting precipitation was washed with ethanol and ultrapure water multiple times and dried in a vacuum environment at 60 °C for 12 h. Finally, the milled product was powdered for subsequent use. For comparison with the synthesis of $Zn_{0.2}Cd_{0.8}S$, a given amount of CDs (0, 0.13, 0.26, and 0.52 mg) prepared in advance according to reference [21] was added for the synthesis of $Zn_{0.2}Cd_{0.8}S@CDs$ (Scheme 1).
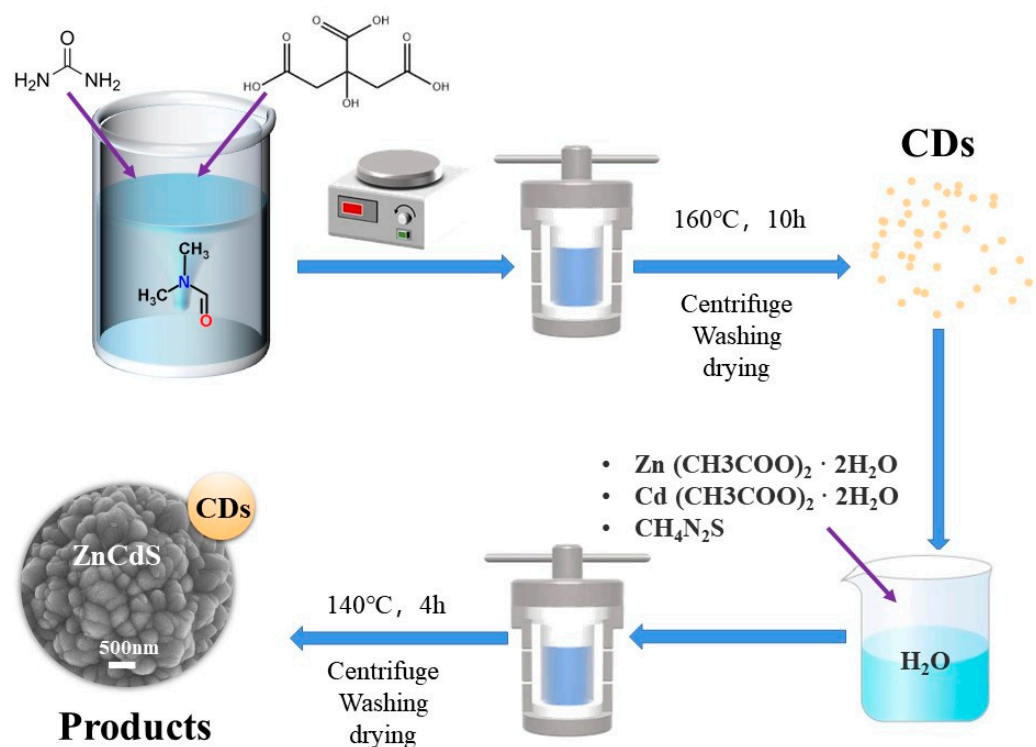
Scheme 1. Schematic diagram of the preparation of $Zn_{0.2}Cd_{0.8}S$ and $Zn_{0.2}Cd_{0.8}S@CDs$.

2.3. Characterization

The samples were characterized by a Hitachi SU8010 scanning electron microscope (SEM). The microstructure was characterized by an FEI-TALOS-F200X transmission electron microscope (TEM). A UL3101-1 atomic force microscope (AFM) was used to characterize the morphology and size of CDs. An FTIR-650 infrared spectrometer and an Ultima IV X-ray diffractometer (XRD) were used to analyze the structure of the samples. The element properties were studied using a Thermo Scientific Kα X-ray photoelectron spectroscope (XPS). UV absorption spectra and UV diffuse reflectance spectra were studied with PerkinElmer and LAMADA950 UV-vis spectrometers. Steady-state, transient fluorescence spectra of samples were obtained with a Hitachi F-4600 photometer. The Mott-Schottky curve, photocurrent response and EIS Nyquist plot were measured on an electrochemical workstation (CHI760E).

The photocatalytic degradation of RhB as a model dye pollutant at room temperature was studied using prepared catalysts in a homemade light reactor using a 500W xenon lamp source. In the experiment, a given amount of photocatalyst was suspended in 500 mL of 10 mg/L RhB solution. In the dark, a magnetic stirrer was used to stir the suspension at a constant speed for 30 min to achieve the adsorption–desorption equilibrium of the dye on the photocatalyst. Then, the suspension was kept in a photocatalytic reactor, the light source was turned on, magnetic stirring was continued, and 5 mL suspension was removed every 30 min and centrifuged at 3000 rpm. The resulting solution was analyzed by a UV-visible spectrophotometer (UV-3150, Shimadzu, Tokyo, Japan) after centrifugation. The concentration of RhB dye was quantified by measuring the absorbance at 553 nm.

The following formula is used to calculate the degradation rate:

$$D(\%) = (C_0 - C)/C_0 \tag{1}$$

where D represents the degradation rate (%), C_0 is the initial concentration of RhB (mg/L), and C is the immediate concentration of RhB every 30 min (mg/L).

3. Results and Discussion

3.1. Morphologic Analysis of the $Zn_{0.2}Cd_{0.8}S@CD$ Catalyst

The morphology of $Zn_{0.2}Cd_{0.8}S$ was observed by SEM. As shown in Figure 1a, the morphology of $Zn_{0.2}Cd_{0.8}S$ shows a nanoflower structure with obvious agglomeration, and the size is approximately 4 μm. Figure 1b shows an enlarged view of a single $Zn_{0.2}Cd_{0.8}S$, which indicates the microstructure. The microstructure of $Zn_{0.2}Cd_{0.8}S$ shows a large specific surface area, which is advantageous for catalytic processes, as it often contains more active catalytic sites [37]. $Zn_{0.2}Cd_{0.8}S$ exhibited a combination of type I and type IV isotherms based on the IUPAC classification [38], indicating a predominance of micropores and mesopores, with an SBET of 4.8945 m^2/g (Figure S1c), possibly because the SBET of nanoflowers composed of columnar granular "petals" is lower than that of nanoflowers composed of flaky "petals". Nevertheless, $Zn_{0.2}Cd_{0.8}S@CDs$ still exhibited high catalytic activity. Owing to the small size of CDs, their microstructure was characterized by TEM. It is evident from Figure 1c that the CDs are evenly spaced out and have diameters between 3 and 4 nm. Figure 1d is a TEM map of $Zn_{0.2}Cd_{0.8}S@CDs$, showing that CD nanoparticles successfully attach to $Zn_{0.2}Cd_{0.8}S$. The close interaction between $Zn_{0.2}Cd_{0.8}S@CDs$ reveals the fast transfer of interface charge and a reduction in the recombination of photogenerated carriers. However, the $Zn_{0.2}Cd_{0.8}S$ catalyst may also be too thick for electrons to penetrate, resulting in black areas in the TEM map. Figure S1a shows that CDs are uniformly dispersed, which is consistent with the TEM results. The size of the synthetic CDs increased slightly due to agglomeration (Figure S1b).
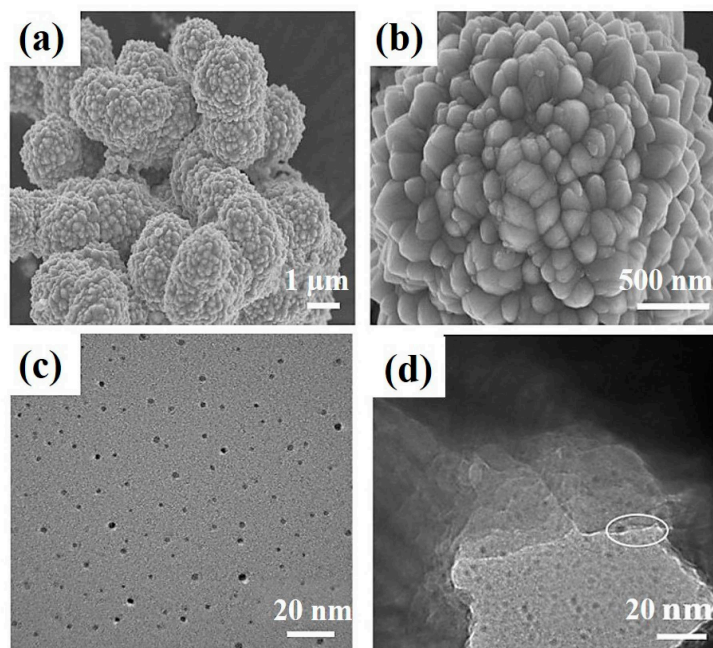
Figure 1. (**a**,**b**) SEM image of $Zn_{0.2}Cd_{0.8}S$; (**c**) TEM image of CDs; (**d**) TEM image of $Zn_{0.2}Cd_{0.8}S@CDs$.

3.2. Structural Analysis of the $Zn_{0.2}Cd_{0.8}S@CD$ Catalyst

The XRD patterns of the prepared $Zn_{0.2}Cd_{0.8}S$ and the resulting $Zn_{0.2}Cd_{0.8}S@CDs$ are depicted in Figure 2. The diffraction peaks of $Zn_{0.2}Cd_{0.8}S$ are strong and narrow, which shows very strong crystallinity. The diffraction peaks at $25.19°$, $26.62°$, $28.16°$, $43.56°$, $47.99°$, and $51.95°$ correspond to the crystal faces of $Zn_{0.2}Cd_{0.8}S$ (100), (002), (101), (110), (103), and (200). The addition of CDs has little effect on the lattice of $Zn_{0.2}Cd_{0.8}S$ (Figure 2a) because the surface coupling of CDs has no significant effect on the intrinsic optical properties of $Zn_{0.2}Cd_{0.8}S$. CDs are most likely present on the surface of $Zn_{0.2}Cd_{0.8}S$ nanoparticles rather than doped into the $Zn_{0.2}Cd_{0.8}S$ lattice. In addition, the average particle size of the obtained nanoparticles was preliminarily calculated using the Debye–Scherrer formula based on the X-ray diffraction results. In the formula, $D = k\lambda/\beta Cos\theta$, D is the mean particle size (nm), λ is the wavelength of the X-ray source (1.5406 A for Cu $k\alpha$), k is Debye–Scherrer constant (0.94), β is the full width at half maximum (FWHM) of the diffraction peaks, and θ is half of the diffraction angle. The calculated diameter of $Zn0.2Cd0.8S$ and $Zn0.2Cd0.8S@CDs$ nanoparticles is estimated to be 25.7 and 33.9 nm, respectively [24,25]. The UV-vis absorption spectrum of CDs in Figure 2b shows that the maximum absorption wavelength of CDs is 365 nm under UV irradiation, and at this wavelength, the CD solution exhibits a strong red fluorescence (as shown in the illustration).

The measured FTIR spectra of CDs, $Zn_{0.2}Cd_{0.8}S$, and $Zn_{0.2}Cd_{0.8}S@CDs$ are shown in Figure 2c,d, respectively. Specifically, tensile vibration peaks of O–H and N–H can be observed in Figure 2c at approximately $3400\ cm^{-1}$ and $3200\ cm^{-1}$, respectively, tensile vibration peaks of C–H at approximately $2900\ cm^{-1}$. The characteristic peak of the C=O bond appears at $1666\ cm^{-1}$. The typical peak of the C=N bond appears at $1446\ cm^{-1}$, and the typical peak of the C–N bond appears at $1612\ cm^{-1}$ due to the synthesis of CDs using DMF as a solvent. The characteristic peak of C–O occurs at $1186\ cm^{-1}$, indicating that there are many hydroxyl groups in the structure of fluorescent CDs. Figure 2d shows that the infrared spectrum of the composite $Zn_{0.2}Cd_{0.8}S@CDs$ is approximately the same as that of $Zn_{0.2}Cd_{0.8}S$. The O–H stretching vibration peak is at approximately $3440\ cm^{-1}$. The peaks at $2950\ cm^{-1}$ and $2856\ cm^{-1}$ represent the stretching vibration of C–H. The tensile vibration peak of C=O occurs at $1623\ cm^{-1}$, and the stretching vibration peak of C–OH occurs at $1378\ cm^{-1}$, both of which are associated with cadmium acetate and zinc acetate. However, the peak of $Zn_{0.2}Cd_{0.8}S@CDs$ at $1450\ cm^{-1}$, which is a C–N stretching vibration

peak, is higher than the peak of $Zn_{0.2}Cd_{0.8}S$. Furthermore, the peak of CDs at 560 cm^{-1} also appears in the infrared spectrum of $Zn_{0.2}Cd_{0.8}S@CDs$, which means the CDs were successfully complexed with $Zn_{0.2}Cd_{0.8}S$.
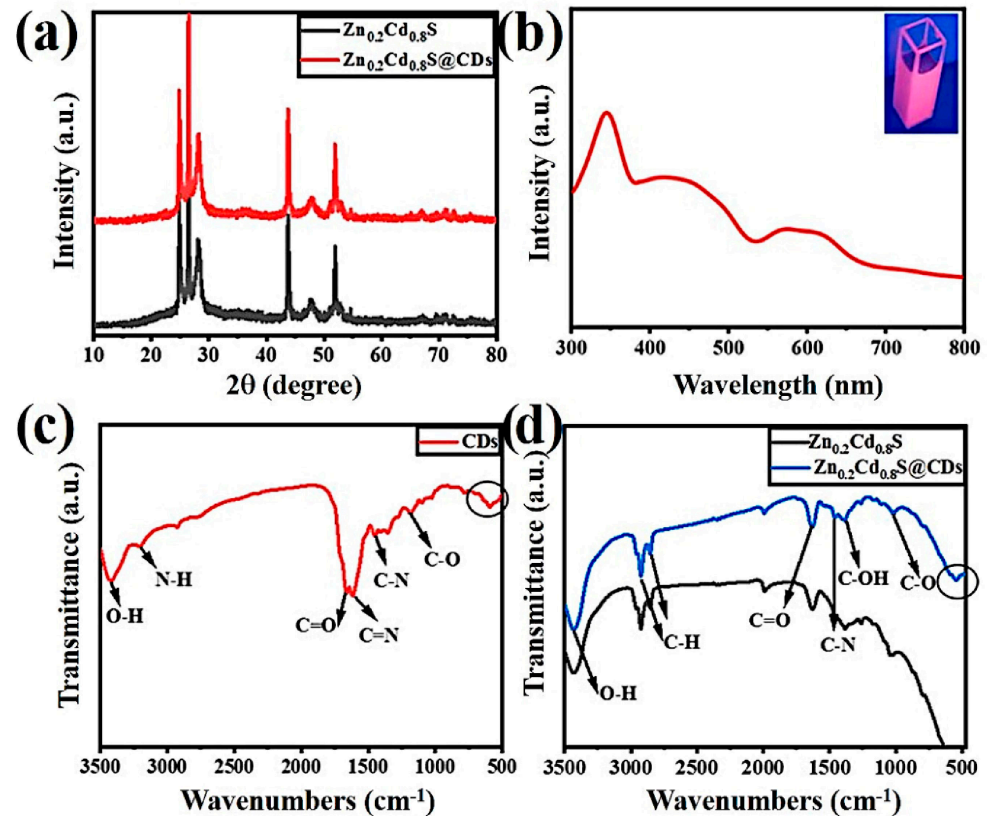
Figure 2. (**a**) XRD patterns of $Zn_{0.2}Cd_{0.8}S$ and $Zn_{0.2}Cd_{0.8}S@CDs$; (**b**) UV-vis spectra of CDs; (**c**,**d**) FTIR spectrum of $Zn_{0.2}Cd_{0.8}S$ CDs and $Zn_{0.2}Cd_{0.8}S@CD$ composite.

Figure 3a shows the XPS full spectrum of the $Zn_{0.2}Cd_{0.8}S@CD$ complex, showing the presence of Zn, Cd, S, C, N, and O elements in the composite, which is very close to the XPS full spectrum of $Zn_{0.2}Cd_{0.8}S$ (Figure S3a). In the high-resolution O 1s spectrum of $Zn_{0.2}Cd_{0.8}S@CDs$ (Figure 3b), the peaks at 531.6 and 533.0 eV are attributed to the C–O and CO bonds, respectively, with some negative shifts compared to Figure S2c, and this shift may be caused by the strong electron interaction between $Zn_{0.2}Cd_{0.8}S$ and CDs. In the high-resolution N 1s spectrum (Figure 3c), the peak located at 404.6 eV corresponds to the amino peak. The N 1s binding energy of $Zn_{0.2}Cd_{0.8}S@CDs$ is greatly increased compared to the N 1s spectrum of CDs (Figure S2d), indicating some coupling between $Zn_{0.2}Cd_{0.8}S$ and CDs. This contributes to the effective interfacial charge separation and transfer between $Zn_{0.2}Cd_{0.8}S$ and CDs. Figure 3d shows that C1s can be divided into four peaks: 284.3 eV, 285.8 eV, 286.5 eV, and 288.4 eV, corresponding to a C–C/C=C bond, C–N bond, C–O bond, and C=O/C=N bond, respectively. The corresponding peaks at the C–N, C–O, and C=O/C=N bonds are weakened compared to the C1s spectrum in Figure S2b, which indicates that some carbon-containing functional groups were removed during the hydrothermal process. The binding energies of Cd 3d3/2 (Figure S3c) and S 2p1/2 (Figure S3d) in the complexes are slightly shifted by 0.1 eV compared to pure $Zn_{0.2}Cd_{0.8}S$, with enhanced binding energy, indicating that electrons are lost and transferred to CDs.

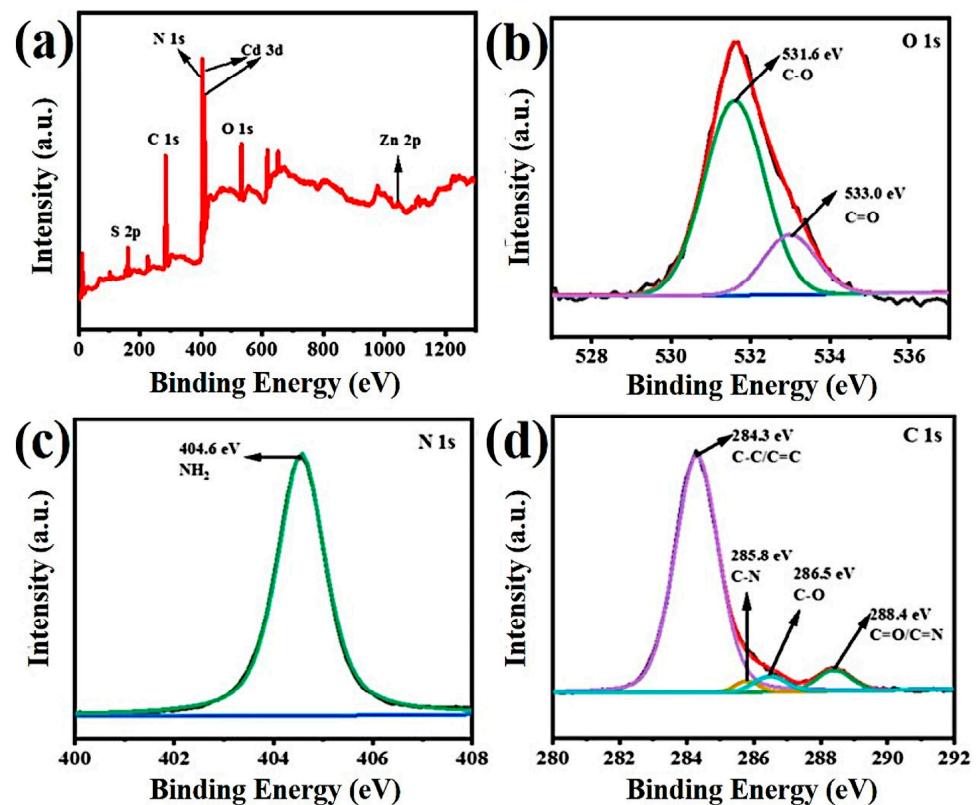**Figure 3.** (**a**) Full scan XPS spectrum of the $Zn_{0.2}Cd_{0.8}S@CD$ composite; high-resolution XPS O 1s; (**b**) N 1s; (**c**) C 1s; (**d**) spectrum of $Zn_{0.2}Cd_{0.8}S@CDs$.

UV-Vis DRS spectroscopy was used to study the light absorption capacity of photocatalysts. Figure 4a shows the light absorption capacity information of $Zn_{0.2}Cd_{0.8}S$ and $Zn_{0.2}Cd_{0.8}S@CDs$. $Zn_{0.2}Cd_{0.8}S$ and $Zn_{0.2}Cd_{0.8}S@CDs$ have strong light-trapping ability in the 200–550 nm wavelength range. To some extent, the light-trapping ability of $Zn_{0.2}Cd_{0.8}S@CDs$ is better than that of $Zn_{0.2}Cd_{0.8}S$. According to the Formulas (2) and (3) shown below, the band gaps of three catalysts were obtained from the Tauc curve [26,27]:

$$(\alpha h v)^{1/2} = K \left(h v - E_g \right) \tag{2}$$

$$h v = 1240/\lambda \tag{3}$$

where α is absorption coefficient, h is the Planck constant, v is the frequency, K is the constant, E_g is the semiconductor bandgap width, and λ is wavelength (nm).
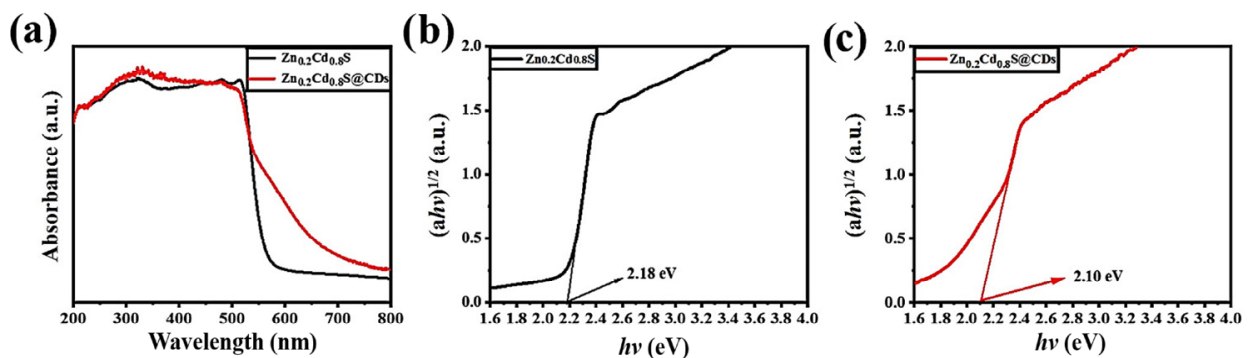

Figure 4. (**a**) UV-Vis DRS absorption spectra of $Zn_{0.2}Cd_{0.8}S$ and $Zn_{0.2}Cd_{0.8}S@CDs$; Band gap energy of (**b**) $Zn_{0.2}Cd_{0.8}S$ and (**c**) $Zn_{0.2}Cd_{0.8}S@$ CDs.

The band gaps of $Zn_{0.2}Cd_{0.8}S$ and $Zn_{0.2}Cd_{0.8}S@CDs$ are 2.18 eV (Figure 4b) and 2.10 eV (Figure 4c), respectively, indicating that CDs are more easily activated from the conduction band to the valence band and enhance the efficient utilization of light by $Zn_{0.2}Cd_{0.8}S$.

The recombination of electron holes and the electron transfer rate in photocatalytic materials were investigated by transient photocurrent and electrochemical impedance measurements (Figure S4). The effect of different contents of CDs on the photocatalytic properties of $Zn_{0.2}Cd_{0.8}S@CDs$ can be obtained from Figure 5a,b. Figure 5a shows that the intensity of instantaneous photocurrent increases first and then decreases with an increase in CD content. Low resistance makes the electrons transfer faster when they are excited, resulting in low electron-hole recombination efficiency. As shown in Figure 5b, the arc radius of the Nyquist graph decreases first and then increases with an increase in the amount of added CDs, which means that the changing trend of electrode resistance decreases first and then increases. The smallest semicircle in the figure corresponds to 0.26 mg of added CDs is, indicating that $Zn_{0.2}Cd_{0.8}S@CDs$ have the lowest electron transfer resistance and the highest electron transfer rate.

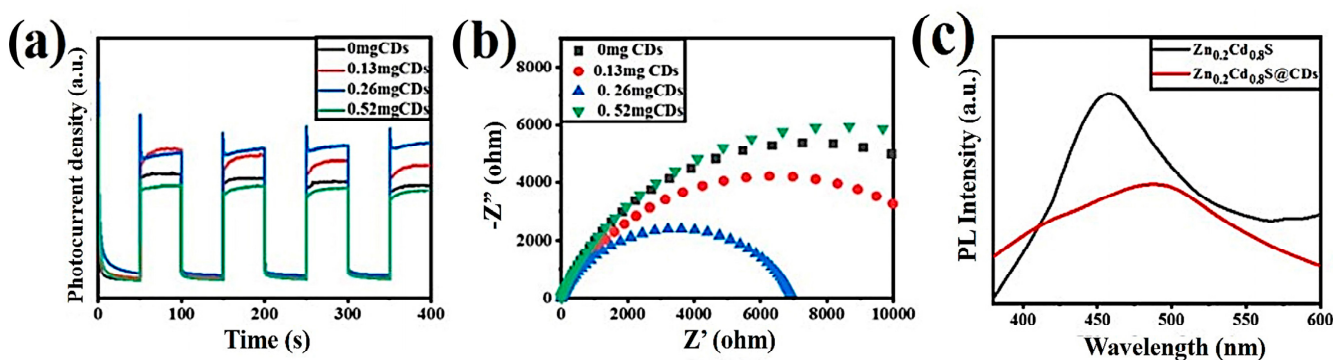**Figure 5.** (**a**) Instantaneous photocurrent diagram of Zn0.2Cd0.8S@CDs with changes in the quantity of CDs quantity; (**b**) electrochemical impedance diagram of Zn0.2Cd0.8S@CDs with changes in the quantity of CDs; (**c**) steady-state fluorescence spectra of Zn0.2Cd0.8S and Zn0.2Cd0.8S@CDs.

Information about separation and transfer of charge and electron-hole recombination in a photocatalyst can be obtained by PL spectra. The PL intensity is positively correlated with the electron-hole recombination rate; the lower the catalyst's fluorescence intensity, the higher the photocatalytic activity [39]. As shown in Figure 5c, $Zn_{0.2}Cd_{0.8}S$ has a significant PL peak at 457 nm. This higher strength indicates that the electron-hole recombination $Zn_{0.2}Cd_{0.8}S$ of is more obvious. However, the fluorescence intensity of the composite catalyst with CDs is lower, which means that the photoexcited electrons transfer from the catalyst to the CDs, indicating that there is less recombination of electrons and holes in $Zn_{0.2}Cd_{0.8}S@CDs$. The coupling between CDs and $Zn_{0.2}Cd_{0.8}S$ provides a fast electron transfer pathway, which improves the photocatalytic properties of $Zn_{0.2}Cd_{0.8}S@CDs$ composites.

3.3. Study of Photocatalytic Degradation of RhB

The absorbance of the solution containing RhB was measured at a wavelength of 553 nm using a UV-Vis spectrophotometer (Figure S5a). A graph of the absorbance at a wavelength of 553 nm versus RhB concentration is shown in Figure S5b. It is obvious that the curve fits the standard curve of the first-order function, and the linear fitting Equation (4) was obtained for subsequent calculation of the degradation rate and instant concentration of RhB:

$$Y = 0.20353X + 0.077 \tag{4}$$

where X is the instant concentration of RhB, and Y is the absorbance of RhB at a wavelength of 553 nm.

The absorbance of the RhB solution containing 30 mg of $Zn_{0.2}Cd_{0.8}S@CDs$ (Figure 6a) and $Zn_{0.2}Cd_{0.8}S$ (Figure 6b) decreased every half hour as a result of the degradation of RhB.

In Figure 6c, the $Zn_{0.2}Cd_{0.8}S@CD$ composite catalyst shows strong adsorption performance under the condition of a dark adsorption equilibrium. The degradation rate of RhB was 12.60% in the RhB-$Zn_{0.2}Cd_{0.8}S@CD$ solution but only 5.70% in RhB-$Zn_{0.2}Cd_{0.8}S$ solution. In addition, it should be emphasized that the degradation rate of RhB in RhB-$Zn_{0.2}Cd_{0.8}S@CD$ solution was higher within 0–1.5 h than that after 1.5 h–2 h, which indicates that the effect of photocatalysis was maximized. The final degradation rate of RhB was 71.3% in RhB-$Zn_{0.2}Cd_{0.8}S@CD$ solution but reached only 59.60% in RhB-$Zn_{0.2}Cd_{0.8}S$ solution after two-hour irradiation. As shown in Figure 6d, under the condition of dark equilibrium adsorption, adding $Zn_{0.2}Cd_{0.8}S@CD$ catalyst resulted in a more significant decrease in the concentration of RhB than adding $Zn_{0.2}Cd_{0.8}S$. The result of the photocatalytic experiments show that the photocatalytic efficiency of the composite catalyst is always higher than that of the single catalyst, which was negatively correlated with the concentration change of RhB. The final concentration of RhB was 4.04 mg/L in RhB-$Zn_{0.2}Cd_{0.8}S$ solution and 2.86 mg/L in RhB-$Zn_{0.2}Cd_{0.8}S@CD$ solution. It can be concluded that the combination of $Zn_{0.2}Cd_{0.8}S$ and CDs can improve the separation of photogenerated electron-hole pairs, as well as the ability to collect visible light and effective photodegradation of RhB.
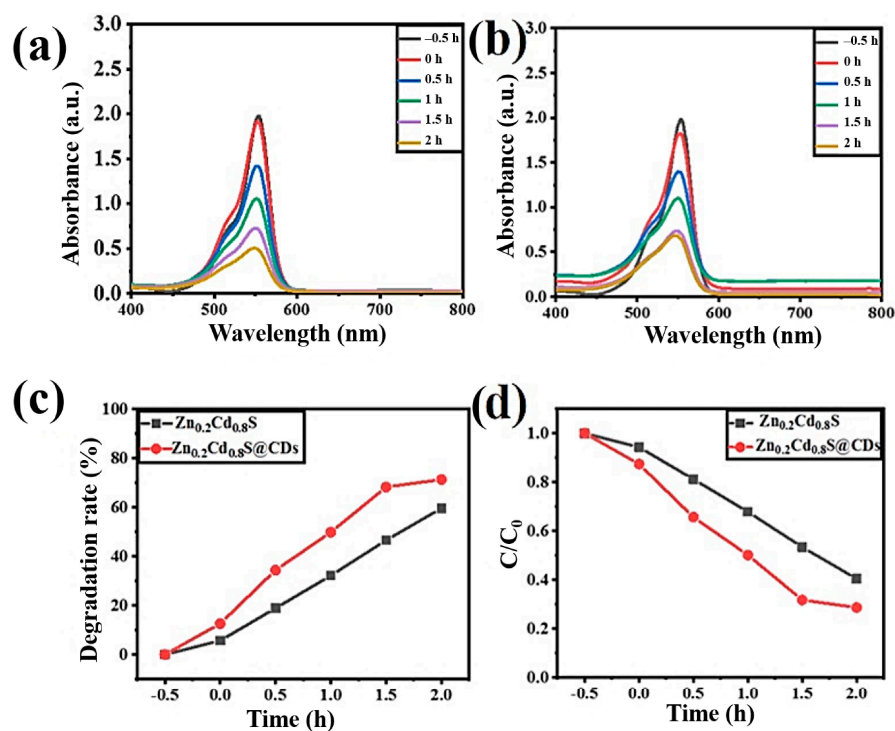

Figure 6. The intensity of the absorption peaks of RhB dye in the presence of $Zn_{0.2}Cd_{0.8}S@CDs$ (**a**) and $Zn_{0.2}Cd_{0.8}S$ (**b**) varies with time. (**c**) The degradation rate of RhB varies with time under the action of catalysts. (**d**) The concentration rate of RhB varies with time under the action of catalysts.

We explored the effects of different dosages of $Zn_{0.2}Cd_{0.8}S@CDs$ (10 mg, 30 mg, 50 mg, and 70 mg) on the photocatalytic degradation ability of RhB. As shown in Figure 7a, the degradation rate of RhB first increased and then decreased with increased content of $Zn_{0.2}Cd_{0.8}S@CDs$ after two-hour irradiation. The highest degradation of RhB was caused by 50 mg of $Zn_{0.2}Cd_{0.8}S@CDs$. Furthermore, as shown in Figure 7b, when the dosage of $Zn_{0.2}Cd_{0.8}S@CDs$ was 50 mg, the concentration of RhB solution was the lowest after irradiation for 2 h. These results indicate that 50 mg of $Zn_{0.2}Cd_{0.8}S@CDs$ had the most obvious photocatalytic degradation effect on RhB. The increased dosages of $Zn_{0.2}Cd_{0.8}S@CDs$ provided more active sites and thus improved the efficiency of photocatalytic degradation of RhB. However, with continued addition of catalyst, the $Zn_{0.2}Cd_{0.8}S@CDs$ particles began to aggregate, resulting in the active sites becoming covered and inactivated in the solution.

The above results indicate that the selection of appropriate catalyst content can effectively improve the photocatalytic degradation performance of $Zn_{0.2}Cd_{0.8}S@CDs$.
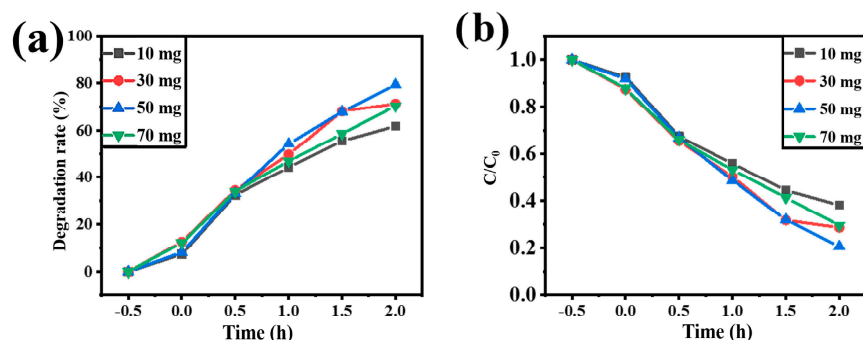

Figure 7. (**a**) Curves of the degradation rate of RhB with different dosages of $Zn_{0.2}Cd_{0.8}S@CD$ photocatalyst over time; (**b**) concentration curves of RhB with different dosages of $Zn_{0.2}Cd_{0.8}S@CDs$ photocatalyst over time.

3.4. Mechanism Exploration

Figure 8 shows the photocatalytic degradation mechanism of RhB under simulated direct sunlight. Valence electrons of $Zn_{0.2}Cd_{0.8}S$ are excited when $Zn_{0.2}Cd_{0.8}S$ is irradiated by sunlight. They move towards the conduction band of $Zn_{0.2}Cd_{0.8}S$, forming electron-hole pairs [28,29]. In general, photoinduced electrons and holes tend to recombine as quickly as possible, and only a limited number of electrons and holes is available for photocatalytic reactions. The doping of CDs accelerates the transfer of electrons and reduces the recombination of electron holes. Then, electrons transfer from the $Zn_{0.2}Cd_{0.8}S$ conduction band to CDs and react with adsorbed O_2 to obtain a superoxide radical ($\bullet O^{2-}$). The valence band holes in $Zn_{0.2}Cd_{0.8}S$ react with the adsorbed H_2O molecules to generate hydroxyl radicals ($\bullet OH$). These hyperactive free radicals are the main reason for the effective degradation of RhB [30]. CDs plays an important role in the entire photocatalytic system; with excellent upconversion performance, they can absorb long-wavelength light and convert it into short-wavelength light, continuously provide efficient absorption of $Zn_{0.2}Cd_{0.8}S$, and greatly improve the utilization rate of solar energy [31]. The raw materials used to prepare CDs are citric acid and urea, which are abundant in N. More N-doped CDs can effectively induce charge delocalization and enhance photocatalytic activity [32]. In conclusion, a CD-based composite catalyst enhances the degradation of RhB to a certain extent, leading to a decrease in electron-hole recombination probability and the acceleration of charge transfer [33].
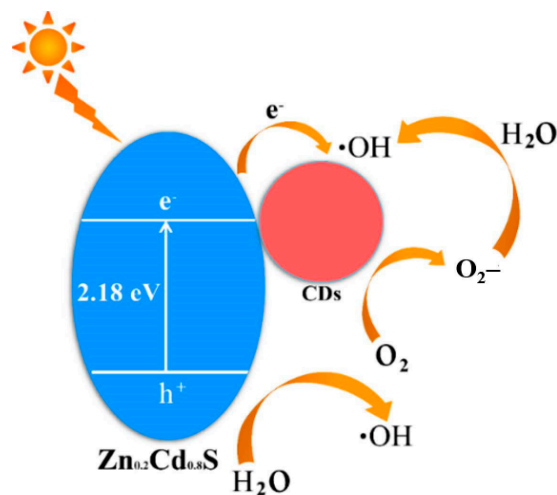

Figure 8. Schematic diagram of charge separation and transfer in $Zn_{0.2}Cd_{0.8}S@CDs$.

4. Conclusions

In summary, to improve the defects of $Zn_{0.2}Cd_{0.8}S$, such as fast recombination of electron-hole pairs and low absorption of visible light, a $Zn_{0.2}Cd_{0.8}S@CDs$ composite catalyst was synthesized by a simple one-pot hydrothermal method with CDs as additives. The doping of CDs inhibits the recombination of electron holes, enhances the electron transfer rate, and enhances the absorption efficiency of light. The most appropriate content of CDs in the $Zn_{0.2}Cd_{0.8}S@CD$ composite catalyst was 0.26 mg. The photocatalytic activity of the $Zn_{0.2}Cd_{0.8}S@CD$ composite catalyst was evaluated by photocatalytic degradation of RhB. The degradation rate of RhB with 30 mg of $Zn_{0.2}Cd_{0.8}S@CD$ catalyst reached 71.36%, whereas that with 30 mg of $Zn_{0.2}Cd_{0.8}S$ catalyst was only 59.60%. The degradation rate of RhB with 50 mg of $Zn_{0.2}Cd_{0.8}S@CDs$ reached 79.35%, which was better than that with other photocatalysts [34–36]. We hope that this work will lead to promising designs of novel co-photocatalysts, as well as applications in water purification by using solar visible-light photocatalysis.

Supplementary Materials: The following supporting information can be downloaded at: https://www.mdpi.com/article/10.3390/ma16010366/s1, Figure S1: AFM image and N_2 adsorption–desorption isotherms; Figure S2: High-resolution XPS spectrum of carbon dots; Figure S3: High-resolution XPS spectrum of ZnCdS; Figure S4: Instantaneous photocurrent diagram; Figure S5: Absorbance curve of rhodamine B.

Author Contributions: Writing—original draft preparation and data curation, J.Z.; formal analysis and data curation, X.Z. (Xin Zhao); data curation, H.X.; writing—review and editing, Z.W.; writing—review and editing and supervision, X.Z. (Xiaoyuan Zhang); supervision, and writing—review and editing, Z.S. All authors have read and agreed to the published version of the manuscript.

Institutional Review Board Statement: Not applicable.

Informed Consent Statement: Not applicable.

Conflicts of Interest: The authors declare no conflict of interest.

References

1. Rao, W.; Piliouras, P.; Wang, X.; Guido, A.; Kugler, K.; Sieren, B.; Wang, L.; Lv, G.; Li, Z. Zwitterionic dye rhodamine B (RhB) uptake on different types of clay minerals. *Appl. Clay Sci.* **2020**, *197*, 105790. [CrossRef]
2. Sun, D.; Yang, X. Rapid Determination of Toxic Rhodamine B in Food Samples Using Exfoliated Graphene-Modified Electrode. *Food Anal. Methods* **2017**, *10*, 2046–2052. [CrossRef]
3. Zhang, T.; Zhou, T.; He, L.; Xu, D.; Bai, L. Oxidative degradation of Rhodamine B by Ag@CuO nanocomposite activated persulfate. *Synth. Met.* **2020**, *267*, 116479. [CrossRef]
4. Xu, Y.; Hu, E.; Xu, D.; Guo, Q. Activation of peroxymonosulfate by bimetallic CoMn oxides loaded on coal fly ash-derived SBA-15 for efficient degradation of Rhodamine B. *Sep. Purif. Technol.* **2021**, *274*, 119081. [CrossRef]
5. Wu, J.; Zhu, K.; Xu, H.; Yan, W. Electrochemical oxidation of rhodamine B by PbO_2/Sb-SnO_2/TiO_2 nanotube arrays electrode. *Chin. J. Catal.* **2019**, *40*, 917–927. [CrossRef]
6. Dai, Q.; Jiang, L.; Luo, X.B. Electrochemical oxidation of rhodamine B: Optimization and degradation mechanism. *Int. J. Electrochem. Sci.* **2017**, *12*, 4265–4276. [CrossRef]
7. Guo, S.; Yang, Z.; Wen, Z.; Fida, H.; Zhang, G.; Chen, J. Reutilization of iron sludge as heterogeneous Fenton catalyst for the degradation of rhodamine B: Role of sulfur and mesoporous structure. *J. Colloid Interface Sci.* **2018**, *532*, 441–448. [CrossRef]
8. Nguyen, L.H.; Van, H.T.; Ngo, Q.N.; Thai, V.N.; Hoang, V.H.; Hai, N.T.T. Improving Fenton-like oxidation of Rhodamin B using a new catalyst based on magnetic/iron-containing waste slag composite. *Environ. Technol. Innov.* **2021**, *23*, 101582. [CrossRef]
9. Liu, P.; Zhong, D.; Xu, Y.; Zhong, N.; He, G. Co/Fe co-doped porous graphite carbon derived from metal organic framework for microelectrolysis-Fenton catalytic degradation of Rhodamine B. *J. Environ. Chem. Eng.* **2021**, *9*, 105924. [CrossRef]
10. Yang, L.; Chen, J.; Liu, X.; Que, M.; Zhao, Y.; Zheng, H.; Yang, T.; Liu, Z.; Li, Y.; Yang, X. 2D/2D BiOBr/(001)-TiO_2 heterojunction toward enhanced photocatalytic degradation activity of Rhodamine B. *J. Alloys Compd.* **2021**, *884*, 161064. [CrossRef]

11. Hu, L.; Mao, D.; Yang, L.H.; Zhu, M.S.; Fei, Z.H.; Sun, S.X.; Fang, D. In2S3 nanoparticles coupled to In-MOF nanorods: The structural and electronic modulation for synergetic photocatalytic degradation of Rhodamine B. *Environ. Res.* **2022**, *203*, 111874. [CrossRef] [PubMed]

12. Elsayed, M.H.; Jayakumar, J.; Abdellah, M.; Mansoure, T.H.; Zheng, K.; Elewa, A.M.; Chang, C.-L.; Ting, L.-Y.; Lin, W.-C.; Yu, H.H.; et al. Visible-light-driven hydrogen evolution using nitrogen-doped carbon quantum dot-implanted polymer dots as metal-free photocatalysts. *Appl. Catal. B Environ.* **2021**, *283*, 119659. [CrossRef]

13. Yan, Z.; Yang, M.; Chen, Y.; Li, T.; Jing, Q.; Liu, P. Hydroxyl-Rich Porous Silica Nanosheets Decorated with Oxygen-Doped Carbon Nitride Nanoparticles for Photocatalytic Degradation of Rhodamine B. *ACS Appl. Nano Mater.* **2022**, *5*, 818–831. [CrossRef]

14. Zeng, R.; Sun, Z.; Cao, S.; Shen, R.; Liu, Z.; Xiong, Y.; Long, J.; Zheng, J.; Zhao, Y.; Shen, Y.; et al. Facile synthesis of Ag-doped ZnCdS nanocrystals and transformation into Ag-doped ZnCdSSe nanocrystals with Se treatment. *RSC Adv.* **2015**, *5*, 1083–1090. [CrossRef]

15. Ding, J.; Wang, H.; Luo, Y.; Xu, Y.; Liu, J.; Lin, R.; Gao, Y.; Lin, Y. Carbon Quantum Dots Modified (002) Oriented Bi$_2$O$_2$CO$_3$ Composites with Enhanced Photocatalytic Removal of Toluene in Air. *Nanomaterials* **2020**, *10*, 1795. [CrossRef] [PubMed]

16. Shen, C.-C.; Liu, Y.-N.; Zhou, X.; Guo, H.-L.; Zhao, Z.-W.; Liang, K.; Xu, A.-W. Large improvement of visible-light photocatalytic H-2-evolution based on cocatalyst-free Zn0.5Cd0.5S synthesized through a two-step process. *Catal. Sci. Technol.* **2017**, *7*, 961–967. [CrossRef]

17. Qin, X.; Cao, R.; Gong, W.; Luo, L.; Shi, G.; Ji, L.; Zhu, A. Hydrothermal growth of ZnCdS/TiO$_2$ nanoparticles on the surface of the Ti$_3$C$_2$ MXene sheet to enhance photocatalytic performance under visible light. *J. Solid State Chem.* **2022**, *306*, 122750. [CrossRef]

18. Kausar, A. Polymer/carbon-based quantum dot nanocomposite: Forthcoming materials for technical application. *J. Macromol. Sci. Part A Pure Appl. Chem.* **2019**, *56*, 341–356. [CrossRef]

19. Wareing, T.C.; Gentile, P.; Phan, A.N. Biomass-Based Carbon Dots: Current Development and Future Perspectives. *ACS Nano* **2021**, *15*, 15471–15501. [CrossRef]

20. Bai, Y.; Yi, X.; Li, B.; Chen, S.; Fan, Z. Constructing porous polyimide/carbon quantum dots aerogel with efficient photocatalytic property under visible light. *Appl. Surf. Sci.* **2022**, *578*, 151993. [CrossRef]

21. Gu, S.; Hsieh, C.-T.; Gandomi, Y.A.; Li, J.; Yue, X.X.; Chang, J.-K. Tailoring fluorescence emissions, quantum yields, and white light emitting from nitrogen-doped graphene and carbon nitride quantum dots. *Nanoscale* **2019**, *11*, 16553–16561. [CrossRef] [PubMed]

22. Huang, G.; Liu, L.; Chen, L.; Gao, L.; Zhu, J.; Fu, H. Unique insights into photocatalytic VOCs oxidation over WO$_3$/carbon dots nanohybrids assisted by water activation and electron transfer at interfaces. *J. Hazard. Mater.* **2022**, *423*. [CrossRef] [PubMed]

23. Ming, H.; Wei, D.; Yang, Y.; Chen, B.; Yang, C.; Zhang, J.; Hou, Y. Photocatalytic activation of peroxymonosulfate by carbon quantum dots functionalized carbon nitride for efficient degradation of bisphenol A under visible-light irradiation. *Chem. Eng. J.* **2021**, *424*, 130296. [CrossRef]

24. Mohammadi, M.; Rezaei, A.; Khazaei, A.; Shu, X.; Zheng, H. Targeted Development of Sustainable Green Catalysts for Oxidation of Alcohols via Tungstate-Decorated Multifunctional Amphiphilic Carbon Quantum Dots. *ACS Appl. Mater. Interfaces* **2019**, *11*, 43796. [CrossRef] [PubMed]

25. Mahmood, A.; Shi, G.; Wang, Z.; Rao, Z.; Xiao, W.; Xie, X.; Sun, J. Carbon quantum dots-TiO$_2$ nanocomposite as an efficient photocatalyst for the photodegradation of aromatic ring-containing mixed VOCs: An experimental and DFT studies of adsorption and electronic structure of the interface. *J. Hazard. Mater.* **2021**, *401*. [CrossRef] [PubMed]

26. Anju; Rais, A.; Rawat, K.; Prasad, T.; Bohidar, H.B. Boron-doped carbon quantum dots: A 'turn-off' fluorescent probe for dopamine detection. *Nanotechnology* **2020**, *32*, 022501. [CrossRef]

27. Lisa John, V.; Joy, F.; Jose Kollannoor, A.; Joseph, K.; Nair, Y.; Vinod, T.P. Amine functionalized carbon quantum dots from paper precursors for selective binding and fluorescent labelling applications. *J. Colloid Interface Sci.* **2022**, *617*, 730–744. [CrossRef]

28. Song, S.; Wu, K.; Wu, H.; Guo, J.; Zhang, L. Multi-shelled ZnO decorated with nitrogen and phosphorus co-doped carbon quantum dots: Synthesis and enhanced photodegradation activity of methylene blue in aqueous solutions. *RSC Adv.* **2019**, *9*, 7362–7374. [CrossRef]

29. Zhu, Z.; Li, X.; Luo, M.; Chen, M.; Chen, W.; Yang, P.; Zhou, X. Synthesis of carbon dots with high photocatalytic reactivity by tailoring heteroatom doping. *J. Colloid Interface Sci.* **2022**, *605*, 330–341. [CrossRef]

30. Dong, Y.; Han, Q.; Hu, Q.; Xu, C.; Dong, C.; Peng, Y.; Ding, Y.; Lan, Y. Carbon quantum dots enriching molecular nickel polyoxometalate over CdS semiconductor for photocatalytic water splitting. *Appl. Catal. B Environ.* **2021**, *293*, 120214. [CrossRef]

31. Athulya, M.; John, B.K.; Chacko, A.R.; Mohan, C.; Mathew, B. A Review on Carbon Quantum Dot Based Semiconductor Photocatalysts for the Abatement of Refractory Pollutants. *Chem. Phys. Chem* **2022**, *23*, e202100873. [CrossRef]

32. Teng, M.; Shi, J.; Qi, H.; Shi, C.; Wang, W.; Kang, F.; Eqi, M.; Huang, Z. Effective enhancement of electron migration and photocatalytic performance of nitrogen-rich carbon nitride by constructing fungal carbon dot/molybdenum disulfide cocatalytic system. *J. Colloid Interface Sci.* **2022**, *609*, 592–605. [CrossRef] [PubMed]

33. Xu, Z.; Wang, Y.; Zhuang, J.; Li, Y.; Jia, L. High temperature hydrothermal etching of g-C$_3$N$_4$ for synthesis of N doped carbon quantum dots-supported CdS photocatalyst to enhance visible light driven hydrogen generation. *Mol. Catal.* **2022**, *517*, 111900. [CrossRef]

34. Bilgic, A. Novel BODIPY-based fluorescent Lycopodium clavatum sporopollenin microcapsules for detection and removal of Cu(II) ions. *Colloids Surf. A Physicochem. Eng. Asp.* **2021**, *631*, 127658. [CrossRef]

35. Bilgic, A. Fabrication of monoBODIPY-functionalized Fe$_3$O$_4$@SiO$_2$@TiO$_2$ nanoparticles for the photocatalytic degradation of rhodamine B under UV irradiation and the detection and removal of Cu(II) ions in aqueous solutions. *J. Alloys Compd.* **2022**, *899*, 163360. [CrossRef]
36. Bilgic, A.; Cimen, A.; Kursunlu, A.N. A novel biosorbent functionalized pillar [5]arene: Synthesis, characterization and effective biosorption of Cr(VI). *Sci. Total Environ.* **2023**, *857*, 159312. [CrossRef]
37. Liu, Q.; Duan, Y.; Zhao, Q.; Pan, F.; Zhang, B.; Zhang, J. Direct Synthesis of Nitrogen-Doped Carbon Nanosheets with High Surface Area and Excellent Oxygen Reduction Performance. *Langmuir* **2014**, *30*, 8238–8245. [CrossRef]
38. Sing, K.S.W. Adsorption methods for the characterization of porous materials. *Adv. Colloid Interface Sci.* **1998**, *76–77*, 3–11. [CrossRef]
39. Chen, Y.; Huang, L.; Li, S.; Pan, D. Aqueous synthesis of glutathione-capped Cu$^+$ and Ag$^+$-doped ZnxCd1−xS quantum dots with full color emission. *J. Mater. Chem. C* **2013**, *1*, 751–756. [CrossRef]